Geophys. J. Int. (1991) **104**, 469–477

Generalized ray theory for an Epstein profile

Guy G. Drijkoningen
Bullard Laboratories, University of Cambridge, Madingley Rise, Madingley Rd, Cambridge CB3 0EZ, *UK*

Accepted 1990 September 14. Received 1990 September 10; in original form 1990 April 4

SUMMARY

The generalized ray method as extended by Heyman & Felsen is used for investigating an Epstein monotonic transition zone. Such an Epstein profile gives rise to normal turning rays, reversed turning rays and space-domain caustics. These wave species can now all be investigated using a complex integration contour in the forming of the synthetic seismogram. We present numerical results of the method and compare it to Chapman's (WKBJ seismogram) method. The waveforms generally agree well although a DC value difference is sometimes present in the seismograms. During the analysis we show that at the dark side of the caustic the arrival can be interpreted as a contribution due to tunnelling rays.

Key words: generalized ray theory, synthetic seismograms, WKBJ seismogram, **x** caustic.

INTRODUCTION

Generalized ray theory is a well-known method for calculating synthetic seismograms in plane-layered homogeneous media. The method is derived from the Cagniard–de Hoop method (see, e.g., Aki & Richards 1980). However, the latter name refers to an exact method while the former one involves an approximation which relates it more to asymptotic ray theory, i.e, the high-frequency approximation to the wave equation. The use of this approximation has thus the advantage that it relates more directly to the physical properties of rays. Another advantage is that because of the approximation the computation of the seismograms is an order of magnitude faster than using the exact formulation.

The dropping of the exactness becomes even more important when we are going to investigate wave propagation through models with continuously varying wavespeeds or, even more complicated, laterally inhomogeneous media. For these types of media an exact formulation along the line of the Cagniard–de Hoop method will probably be difficult to achieve and be expensive in computational effort, and this is enough reason to adopt an asymptotic approach.

As said before generalized ray theory has conventionally been used for plane-layered homogeneous media. Some attempts have been made to extend the method to inhomogeneous media, see for instance Hong & Helmberger (1977, 1978) who tried to apply the method to media separated from each other by dipping interfaces. Extending the method to media continuously varying in wavespeed in one direction has only recently been achieved by Heyman & Felsen (1984, 1987). Before Heyman & Felsen published their findings, the main stumbling block had been how to deal with the turning ray. Here we hope to explain in a slightly different way why the characteristics are as Heyman & Felsen describe them.

In this paper we shall investigate an example of a so-called Epstein profile. Epstein profiles entail a certain class of velocity models which describe the whole space. These profiles were first discussed rigorously by Epstein (1930) and thus the profiles are called after him. Much of this work has been reviewed in the book by Budden (1961) and in a paper by Phinney (1970). The particular Epstein profile we are interested in here, is the monotonic transition zone. This is an interesting one since it gives rise to turning rays and some associated phenomena such as the reversed turning ray, complex (or tunnelling) ray and a caustic. This profile has been investigated before (Hron & Chapman 1974) but their investigation was fairly numerical and did not give a full physical account of what was happening. It is now clear, using Heyman & Felsen's approach, that we can achieve the same results in a much more robust and quicker way.

We start the discussion with deriving the response function in the frequency–slowness (or wavenumber) domain. In order to be able to invert the result to the space–time domain, i.e., the synthetic seismogram, we use a ray approach so the high-frequency approximation is introduced. We will then apply the method of Heyman & Felsen. Apart from using the complex-contour solutions for the inversion to the space–time domain, we must also determine where these contours lie and why they behave the way as described; this is also discussed. We shall then illustrate the theory with some numerical examples and pinpoint what each peak in the seismogram physically

relates to, in particular the caustic and the complex (or tunnelling) ray.

RESPONSE IN THE FREQUENCY (ω)-SLOWNESS (p) DOMAIN

The configuration we will investigate is given in Fig. 1. The horizontal coordinates are denoted by X and Y and the vertical coordinate by z, the positive axis pointing upwards in a right-handed system. We have a point-source situated on the z axis at a large height z_s, while the receiver is situated at range x and a large height z_r.

Also in Fig. 1 is given the velocity profile under consideration. The transition zone is centred around $z=0$. Far above the transition the wavespeed is α_1 while far below the wavespeed reduces to α_2. The wavespeed α at any depth is given by

$$\alpha = \alpha_1\alpha_2\left(\frac{e^{z/\sigma}+1}{\alpha_2^2 e^{z/\sigma}+\alpha_1^2}\right)^{1/2}, \tag{1}$$

where σ is a parameter controlling the width of the transition zone.

We investigate propagation of acoustic waves through this profile. The source function is taken as a Dirac pulse in time, starting to act at time $t=0$. The field for the pressure P is governed by the inhomogeneous wave equation:

$$\frac{\partial^2 P}{\partial X^2}+\frac{\partial^2 P}{\partial Y^2}+\frac{\partial^2 P}{\partial z^2}-\frac{1}{\alpha^2(z)}\frac{\partial^2 P}{\partial t^2}=-\delta(X, Y, z-z_s)\delta(t). \tag{2}$$

We have ignored any density variations. Phinney (1970) showed how to include such variations but they did not affect the results very significantly. We apply Fourier transformations with respect to the horizontal coordinates and the time according to

$$\tilde{P}(p_X, p_Y, z, \omega)=\int_{-\infty}^{\infty}\!\!\int\!\!\int P(X, Y, z, t) \times \exp\left[i\omega(t-p_X X-p_Y Y)\right] dX\, dY\, dt. \tag{3}$$

This will transform the partial differential equation (2) into an ordinary differential equation in the transform

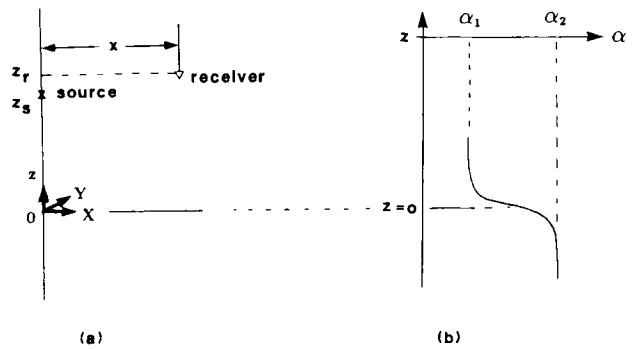

Figure 1. (a) Source–receiver configuration. (b) Epstein profile of monotonic transition zone with middle of transition at $z=0$: $\alpha(z)=\alpha_1\alpha_2(e^{z/\sigma}+1)^{1/2}(\alpha_2^2 e^{z/\sigma}+\alpha_1^2)^{-1/2}$.

(p_X, p_Y, z, ω) domain. We can write it as

$$\frac{d^2\tilde{P}}{dz^2}+\omega^2 q^2(z)\tilde{P}=-\delta(z-z_s) \tag{4}$$

where

$$q^2=\frac{1}{\alpha^2(z)}-p_X^2-p_Y^2. \tag{5}$$

Let us ignore for the moment the source term $\delta(z-z_s)$. This term is easily included by matching the solution of the homogeneous differential equation to the incident-field term. We cannot solve the homogeneous differential equation very easily due to the dependence of the vertical wave slowness q on the vertical coordinate z, but as we will see, we can transform the dependent and independent variables such that we do know the solutions. This can be achieved by letting

$$\tilde{P}=\tilde{\Phi}\exp(i\omega q_2 z) \tag{6}$$

and changing the wave equation into a differential equation in the dependent variable $\tilde{\Phi}$. For the differential equation in $\tilde{\Phi}$ we change the independent variable z to ζ according to

$$-\zeta=e^{z/\sigma}. \tag{7}$$

Working this out gives us a special form of the hypergeometric differential equation:

$$\zeta(1-\zeta)\frac{d^2\tilde{\Phi}}{d\zeta^2}+[c-(a+b+1)\zeta]\frac{d\tilde{\Phi}}{d\zeta}-ab\tilde{\Phi}=0, \tag{8}$$

where for our profile the constants a, b and c take the values

$$a=i\omega\sigma(q_2+q_1), \tag{9}$$

$$b=i\omega\sigma(q_2-q_1), \tag{10}$$

$$c=a+b+1=1+2i\omega\sigma q_2. \tag{11}$$

In these expressions q_1 and q_2 denote the vertical wave slownesses for $\alpha=\alpha_1$ and α_2 respectively. The solutions of the hypergeometric equation are known as hypergeometric functions (F). We shall not go into the details of these functions but only use some properties of them. These can be found in Abramowitz & Stegun (1972, chapter 15). We choose a solution which is of interest to us, i.e.,

$$\tilde{\Phi}=\frac{\Gamma(b-a)\Gamma(1+a-c)}{\Gamma(1-a)}\tilde{\Phi}_1+\frac{\Gamma(a-b)\Gamma(1+b-c)}{\Gamma(1-b)}\tilde{\Phi}_2, \tag{12}$$

where Γ denotes the gamma function and

$$\tilde{\Phi}_1=(-\zeta)^{-a}F(a, 1-c+a; 1-b+a; \zeta^{-1}), \tag{13}$$

$$\tilde{\Phi}_2=(-\zeta)^{-b}F(b, 1-c+b; 1-a+b; \zeta^{-1}). \tag{14}$$

We have taken this special linear combination since we can show that this solution gives rise to a purely downgoing wave below the transition zone. To this effect, we have made use of the so-called circuit relation, see, e.g., Budden (1961). We have chosen this specific solution for our problem but for other ones, such as an incident wave from below the transition zone, another choice must be made. This can be found in Budden (1961).

Far above the transition zone $\zeta(=-e^{z/\sigma})$ is large and the hypergeometric functions (F) above are well approximated by taking them equal to unity. From now on, we can leave

the hypergeometric functions behind us. Taking this approximation, we get for the pressure above the transition zone:

$$\tilde{P} \simeq \frac{\Gamma(b-a)\Gamma(1+a-c)}{\Gamma(1-a)} \exp\left[-i\omega z(q_2+q_1)\right] + \frac{\Gamma(a-b)\Gamma(1+b-c)}{\Gamma(1-b)} \exp\left[-i\omega z(q_2-q_1)\right]. \quad (15)$$

Since the first term represents a downgoing wave and the second an upgoing one, we can determine the reflection coefficient of the region by dividing the second term by the first one;

$$R_D = \frac{q_2+q_1}{q_2-q_1} \frac{\Gamma(2i\omega\sigma q_1)}{\Gamma(-2i\omega\sigma q_1)} \frac{\Gamma^2[-i\omega\sigma(q_2+q_1)]}{\Gamma^2[-i\omega\sigma(q_2-q_1)]} \exp(2i\omega q_1 z). \quad (16)$$

We have established the reflection coefficient of the transition zone which still has the gamma functions in it. This is quite awkward when we want to invert our results to the space–time domain. Therefore we will now approximate the gamma functions by making use of the high-frequency approximation, thus using the asymptotic form for the gamma functions valid for large arguments, also called the Stirling approximation (Abramowitz & Stegun 1972):

$$\Gamma(z) \simeq (2\pi)^{1/2} e^{-z} z^{z-1/2}. \quad \text{(AS6.1.37)}$$

This then finally gives us for the reflection coefficient:

$$R_D \simeq -i \operatorname{sgn}(\omega) \times \exp\left[i\omega\left(2q_1 z + 2\sigma q_1 \ln\frac{4q_1^2}{q_1^2-q_2^2} + 2\sigma q_2 \ln\frac{q_2-q_1}{q_2+q_1}\right)\right]. \quad (17)$$

Note that we have a term $-i \operatorname{sgn}(\omega)$ and a phase term independent of frequency ω. The inclusion of $\operatorname{sgn}(\omega)$ arises due to the same argument as Heyman & Felsen (1984, 1987) use, namely that in order to have a causal signal we must require the amplitude to satisfy

$$A_{\omega>0} = \bar{A}_{\omega<0}, \quad (18)$$

where the bar denotes complex conjugate.

We have solved the homogeneous part of the ordinary differential equation but the last thing we need to do is to match this solution to the incident field. The incident field is easy to determine. Far above the transition zone the vertical wave slowness q is approximately constant, i.e., $q \simeq q_1$ and q no longer depends on z. Then

$$\tilde{P}^{\text{inc}} \simeq \frac{i}{2\omega q_1} \exp(i\omega q_1 |z_s - z_r|), \quad (19)$$

where we have chosen the convention $\mathcal{I}m(\omega q) \geq 0$ in order to have an exponentially decaying wave at infinity.

The final transform-domain solution becomes

$$\tilde{P}(p_X, p_Y, z, \omega) \simeq \frac{i}{2\omega q_1}[-i \operatorname{sgn}(\omega) \exp(i\omega\tau)] \quad (20)$$

where

$$\tau = q_1(z_s+z_r) + 2\sigma q_1 \ln\frac{4q_1^2}{q_1^2-q_2^2} + 2\sigma q_2 \ln\frac{q_2-q_1}{q_2+q_1}. \quad (21)$$

In the next section we will focus on the inversion of this response to the space–time domain.

THE SYNTHETIC SEISMOGRAM

The space–time domain expression for the reflected pressure as derived in the previous section is

$$P(\mathbf{x}, t) = \left(\frac{1}{2\pi}\right)^3 \int\int\int_{-\infty}^{\infty} \frac{\operatorname{sgn}(\omega)}{2\omega q_1} \exp\left[-i\omega(t - p_X X - p_Y Y - \tau)\right] \times \omega |\omega| \, dp_X \, dp_Y \, d\omega. \quad (22)$$

It is now usual to rewrite the integration over p_X and p_Y, see e.g. Aki & Richards (1980). We introduce polar coordinates for the parameters p_X and p_Y, i.e., $p_X = p\cos\psi$ and $p_Y = p\sin\psi$ and also for the coordinates, i.e., $X = x\cos\phi$ and $Y = x\sin\phi$, where x is associated with the range. The integral expression of the Bessel function can then be recognized within the obtained result. We then rewrite the Bessel function in terms of the Hankel functions. In order to be able to use the method of Heyman & Felsen (1984, 1987) we need to take the far-field approximation to the Hankel function as well and we finally obtain

$$P(\mathbf{x}, t) = \frac{1}{8\pi^3} \int\int_{-\infty}^{\infty} \left(\frac{p}{2x}\right)^{1/2} (-i\omega\pi)^{1/2} \frac{1}{q_1} \times \exp\left[-i\omega(t-\theta)\right] dp \, d\omega, \quad (23)$$

where

$$\theta = px + q_1(z_s+z_r) + 2\sigma q_1 \ln\frac{4q_1^2}{q_1^2-q_2^2} + 2\sigma q_2 \ln\frac{q_2-q_1}{q_2+q_1}. \quad (24)$$

Before evaluating this integral we would like to split off one term which comes in as a convolution in the final answer, namely the term $(-i\omega\pi)^{1/2}$. We know that the inverse Fourier transform ($\mathcal{F}_t^{-1}$) of this term is:

$$\mathcal{F}_t^{-1}[(-i\omega\pi)^{1/2}] = \frac{d}{dt}\left[\frac{H(t)}{t^{1/2}}\right], \quad (25)$$

where H denotes the Heaviside step function.

The expression for the pressure is now in a suitable form for inversion using the approach of Heyman & Felsen. To this effect we first evaluate the integral over frequencies by changing the order of integration. The special feature Heyman & Felsen introduced is that they separate the integration over positive and negative frequencies. We then obtain

$$P(\mathbf{x}, t) = \frac{d}{dt}\left[\frac{H(t)}{t^{1/2}}\right] * \frac{-i}{8\pi^3(2x)^{1/2}} \times \left(\int_{-\infty\pm i\epsilon}^{\infty\mp i\epsilon} \frac{p^{1/2}}{t-\theta}\frac{dp}{q_1} - \int_{-\infty\mp i\epsilon}^{\infty\pm i\epsilon} \frac{p^{1/2}}{t-\theta}\frac{dp}{q_1}\right), \quad (26)$$

where ϵ is a small quantity to denote that the paths of integration run infinitesimally above or below the real p axis, dependent on the sign of $d\theta/dp$; the asterisk * here denotes a convolution.

Next, we investigate the contributions of the poles $t = \theta$ to the integrals. Solving $t = \theta$ for p analytically is often, and also in our case, a difficult task so then numerical methods are employed to solve it. What we are able to investigate

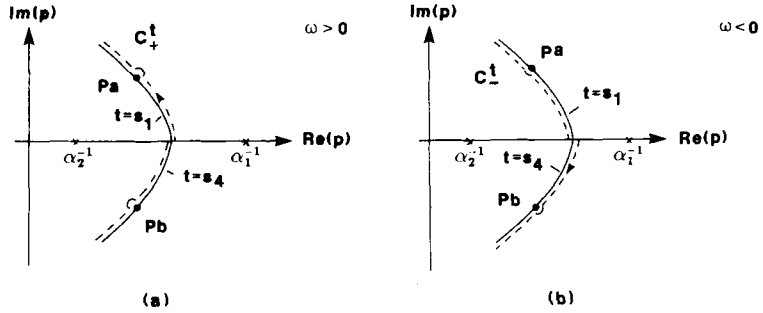

Figure 2. Contour $\theta = s$, $-\infty < s < T_s$ in complex p plane. T_s is saddle-point value. Poles p_a, p_b correspond to $\theta = t (t < T_s)$. s_1 are solutions in first quadrant, s_4 in fourth. $C'_\pm$ (dashed) are deformed paths of integration for positive (a) and negative (b) frequencies.

analytically is the behaviour near characteristic points. In our case such points are saddle points, i.e., the values $p = p_s$ which solve $d\theta/dp = 0$. Let $p = p_s + \varepsilon$. A Taylor expansion about a saddle point gives

$$\theta \simeq \theta|_{p=p_s} + \varepsilon \frac{d\theta}{dp}\bigg|_{p=p_s} + \frac{1}{2}\varepsilon^2 \frac{d^2\theta}{dp^2}\bigg|_{p=p_s} \tag{27}$$

$$= T_s + \frac{1}{2}\varepsilon^2 \frac{d^2\theta}{dp^2}\bigg|_{p=p_s}. \tag{28}$$

Solving for ε gives

$$\varepsilon = 2^{1/2} \frac{(\theta - T_s)^{1/2}}{\left(\dfrac{d^2\theta}{dp^2}\bigg|_{p=p_s}\right)^{1/2}}. \tag{29}$$

This tells us a lot about the behaviour of the contour near the saddle point. Take as a first example a normal turning ray for which $d^2\theta/dp^2|_{p=p_s}$ is larger than zero. This means that if θ (which we will later associate with time t) is larger than T_s, the arrival time of the ray, ε will be purely real. Consequently, we will have solutions on the real p axis for $\theta > T_s$. These solutions are used in Chapman's method (WKBJ seismogram, Chapman 1978). In this paper we are only interested in the real solutions for comparisons; for more details about these solutions within the present framework, see Drijkoningen (1989). When we look at solutions for θ smaller than T_s, ε will be purely imaginary so non-real solutions exist for $\theta < T_s$.

Another example is the reversed turning ray for which $d^2\theta/dp^2|_{p=p_s}$ is smaller than zero. This means that if θ is larger than T_s, the arrival time of the ray, ε will be purely imaginary and we will have non-real solutions for $\theta > T_s$. Again, it is simple to argue that for $\theta < T_s$ we will obtain purely real solutions.

Let us now proceed with the integration over p, considering the case of a normal turning ray, i.e., $d^2\theta/dp^2|_{p=p_s} > 0$. In generalized ray theory we are concerned with the complex solutions of $t = \theta$. A typical contour is given in Fig. 2. We will call the complex solutions $\theta = s$ where s is contained in the interval $-\infty < s < T_s$. We deform the original contours of integration to the complex contour $C'_\pm$ with an arc at infinity. Since the arc at infinity does not contribute we have a Cauchy principal value and two contributions due to the half loops around the poles,

$$\int_{-\infty \mp i\epsilon}^{\infty \pm i\epsilon} \frac{p^{1/2}}{t - \theta q_1}\frac{dp}{} = \frac{\pi i}{q_1}\frac{p^{1/2}}{d\theta/dp}\bigg|_{p=p_b} - \frac{\pi i}{q_1}\frac{p^{1/2}}{d\theta/dp}\bigg|_{p=p_a} + P\int_{C'_\pm} \frac{p^{1/2}}{t - \theta q_1}\frac{dp}{} \tag{30}$$

where p_a and p_b denote the solutions p above and below the real axis respectively, lying on the contours $t = s_1$ and $t = s_4$ respectively; the upper and lower signs correspond to each other. Now adding the two integrals in the expression for the pressure gives only principal-value integrals since the pole contributions cancel. We change the variable of integration from p to θ, and we recognize the integrals as Hilbert transforms. Then we are able to make use of the fact that the solutions s_1 are complex conjugate to the ones on s_4. Finally, we transfer the Hilbert transform operator to the other term in the convolution in order to obtain

$$P(\mathbf{x}, t) = \frac{d}{dt}\left[\frac{H(-t)}{(-t)^{1/2}}\right] * \frac{-1}{2\pi^2}\frac{1}{(2x)^{1/2}}\mathcal{I}m\left(\frac{p^{1/2}}{q_1\, d\theta/dp}\right)_{t=s_4}, \tag{31}$$

where we made use of the fact that the Hilbert transform of $H(t)t^{-1/2}$ is just its time reversal, i.e., $H(-t)(-t)^{-1/2}$. This expression for the pressure P is the final answer we wished to obtain. This is the result due to Heyman & Felsen (1984, 1987).

So far, we looked at the case of a normal turning ray for which $d^2\theta/dp^2$ is larger than zero at the saddle point. For a reversed turning ray the case is slightly different. The solutions and the contours of integration are given in Fig. 3.

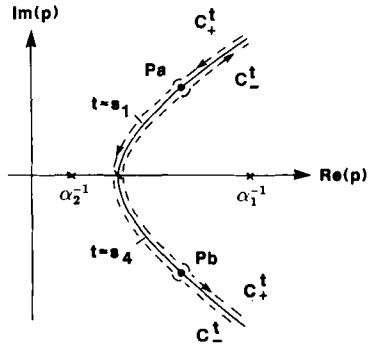

Figure 3. Complex p plane for reversed turning ray ($d^2\theta/dp^2 < 0$ at saddle point). $C'_\pm$ are paths of integration (dashed), s_1 are solutions in first quadrant, s_4 in fourth (drawn).

The analytic continuation is now just opposite to the case of a normal turning ray but it can be shown without much difficulty (following the same procedure as before) that the same result as above will arise.

NUMERICAL EXAMPLES

We start the numerical results with looking at the characteristic points in the complex p plane, namely the (real) saddle points. These are the points of main interest since no branch cuts or poles are present in our problem. Real saddle points are conventionally used in asymptotic ray theory and they will give us traveltime and geometrical spreading of a ray. In Fig. 4 we have plotted the traveltime T as a function of range x for the Epstein transition zone. We see that the traveltime curve forms a triplication. The two special points occurring on this curve are points B and D since there two arrivals merge into one. At the point where the two arrivals merge we are on a caustic.

We have described a certain type of caustic here. It is well known that asymptotic ray theory fails here since the amplitude becomes infinite. However, when we look at the slowness-domain description of this caustic the amplitudes remain finite. This is a result obtained by Maslov (1965, 1972). Less mathematical investigations into this behaviour of caustics have appeared as well, see for instance Chapman & Drummond (1982) and Ziolkowski & Deschamps (1984). The crucial point here is that in a combined 6-D space–slowness domain (phase space) the amplitude will always remain finite. This means that we can always find a subspace (either the space or the slowness domain) where the amplitude remains finite. For the Epstein transition zone, the amplitude becomes infinite in the spatial domain, hence this caustic is called an **x** caustic. For such a caustic, $d^2\theta/dp^2 = 0$. The other type of caustic which may exist but is not encountered in our Epstein problem is the case of a **p** caustic where we have: $d^2\theta/dx^2 = 0$.

As we have seen we have two **x** caustics due to our Epstein profile, characterized by points B and D in the T–x diagram. We first consider the behaviour near the caustic closest to the source (point B). To obtain the synthetic seismogram we must solve $t = \theta$, θ give by (24). As said before, we cannot do this analytically so we must use numerical methods. Let us first look at the solutions in the lit region (point C in the T–x diagram) where two real saddle points exist. The solutions are given in Fig. 5. In Fig. 5(a) we have plotted the real solutions which are used in Chapman's (WKBJ seismogram) method. We can see that the curve has two extrema which correspond to the saddle points. It is well known that Chapman's method gives accurate results for these wave species (Dey-Sarkar & Chapman 1978). In Fig. 5(b) we plotted the complex p solutions. These solutions correspond very well to our description earlier on the behaviour of a normal turning ray ($d^2\theta/dp^2 > 0$ at the saddle point) and a reversed turning ray ($d^2\theta/dp^2 < 0$). It can be seen from the curves in Figs 5(a) and (b) that if we specify one time point t we can find three solutions for p, either all three real, or one real and two complex values, the complex values being the complex-conjugates of each other.

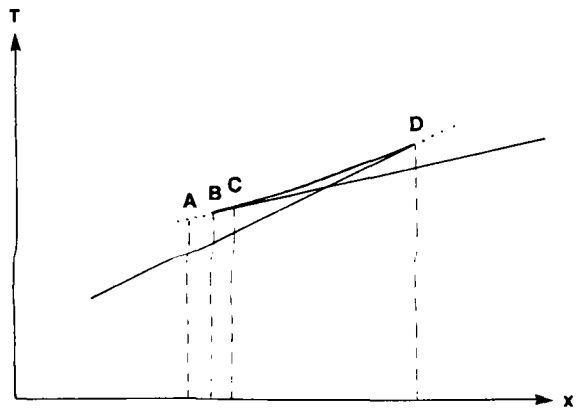

Figure 4. Traveltime T as function of range x for Epstein profile under consideration.

For the numerical evaluation of the synthetic seismogram we still need to smooth both terms in the expression above (31). The first term has a singularity at $t = 0$ and it is necessary to smooth the time series. A way to do this is to convolve the series $d/dt[H(t)t^{-1/2}]$ with a boxcar of the type

$$\frac{1}{2\Delta t}[H(t+\Delta t) - H(t-\Delta t)],$$

where Δt is the sampling width. Chapman & Drummond (1982) applied this filter three times and approximated the discrete time series by a rational approximation. The second term in expression (31) has a singularity at the point where $d\theta/dp$ is zero. We first write

$$\mathcal{H}m\left(\frac{p^{1/2}}{q_1\, d\theta/dp}\right)_{t=\theta} = \int_{-\infty}^{\infty} \delta(t-\theta)\, \mathcal{H}m\left(\frac{p^{1/2}}{q_1}\, dp\right), \tag{32}$$

and then we convolve the integral on the right-hand side with the boxcar filter as given above and we obtain the smooth series:

$$\mathcal{H}m\left(\frac{p^{1/2}}{q_1\, d\theta/dp}\right)_{t=\theta} \simeq \frac{1}{2}\, \mathcal{H}m\left[\left(\frac{p^{1/2}}{q_1(p)}\bigg|_{\theta=t+\Delta t} + \frac{p^{1/2}}{q_1(p)}\bigg|_{\theta=t-\Delta t}\right) \times (p|_{\theta=t+\Delta t} - p|_{\theta=t-\Delta t})\right]. \tag{33}$$

This approach has been used in the numerical examples here since then the results are easily verified against the implementation of the WKBJ seismogram by Chapman, Jen-Yi & Lyness (1988).

We now return to our picture and use either the real or complex solutions in the forming of the synthetic seismogram. This has been done in Fig. 5(c). We see that the turning ray has the usual geometrical ray waveform corresponding to the Dirac pulse while the reversed turning ray has a waveform which is the Hilbert-transformed Dirac pulse ($\sim 1/t$). We have plotted the results from Chapman's and Heyman–Felsen's method on top of each other and we can see that the methods compare very well.

So far, we looked at a range which gave two real saddle-point contributions so we were in the lit region of the caustic. Decreasing the range x a little bit, we will arrive at the range (B in the T–x diagram) where we are at the caustic. The behaviour of such a caustic is well known, see e.g. Jeffreys (1939), Burridge (1963). Using the method employed here we can see that we obtain its behaviour in an

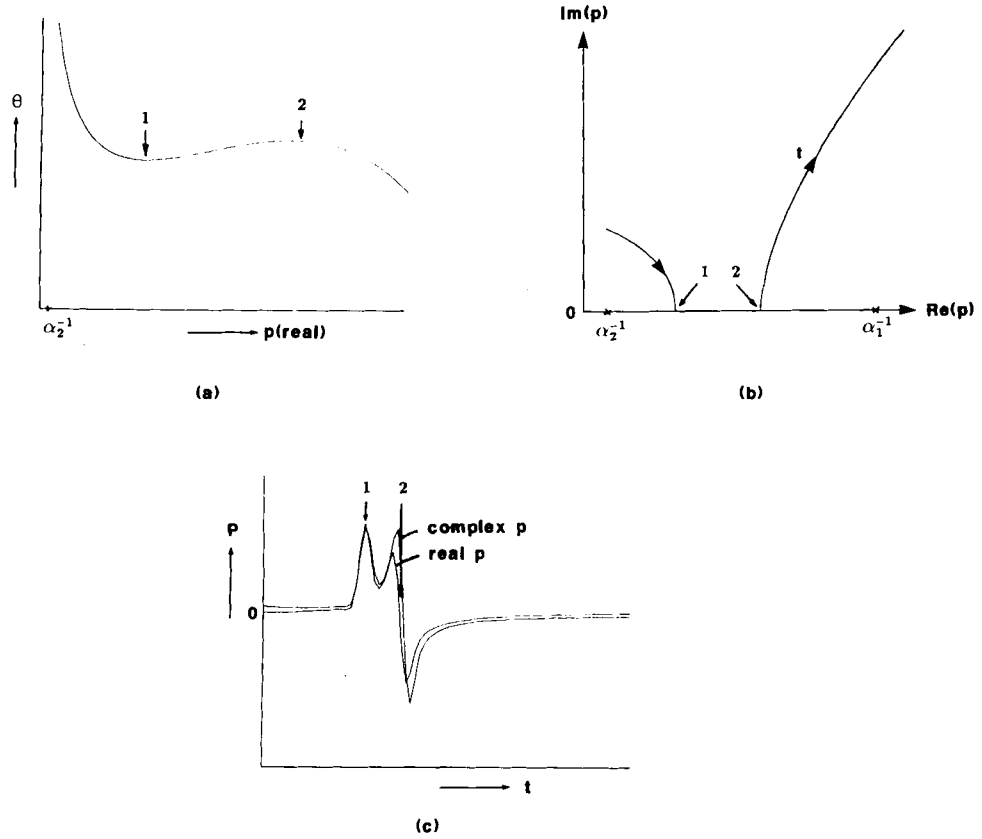

Figure 5. Contours $t = \theta$ at range in lit region of caustic and seismograms associated with it. (a) Real solutions p, (b) complex solutions p, (c) seismograms for real and complex solutions.

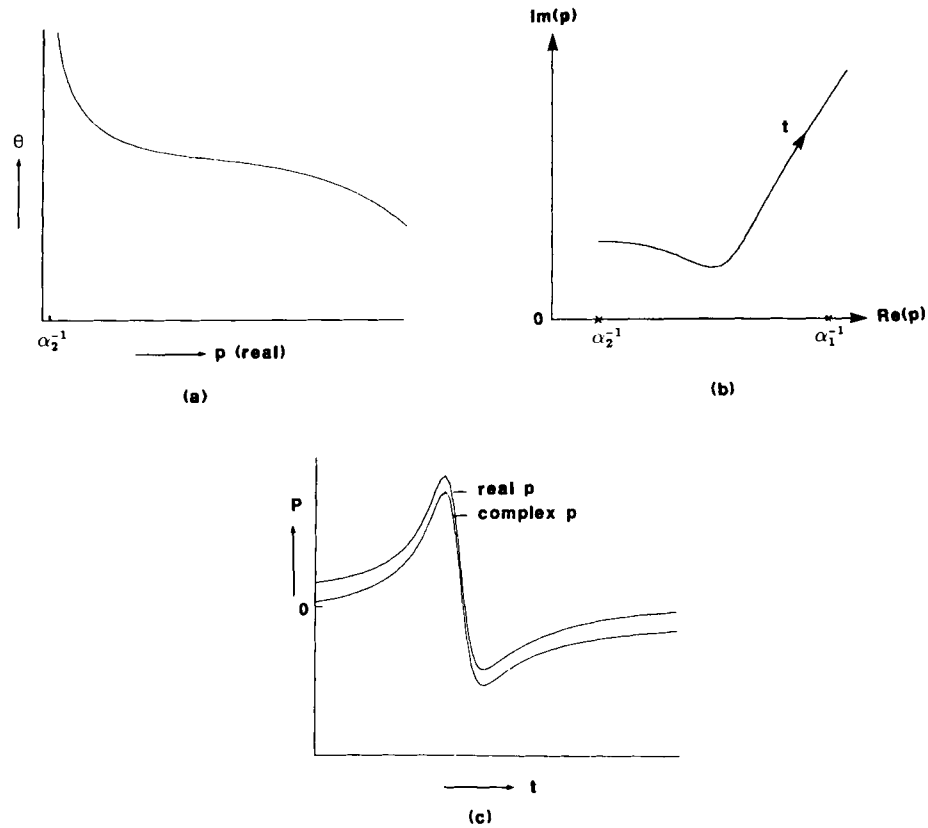

Figure 6. Contours $t = \theta$ at range in dark region of caustic and seismograms associated with it. (a) Real solutions p, (b) complex solutions p, and (c) seismograms for real and complex solutions.

automatic fashion; no special treatment is necessary. At the caustic itself, we can use some analytical approximation in order to check the (automatic) result. Doing this it can be shown that the waveform is the inverse Fourier transform of the Airy function (Burridge 1963; Chapman & Orcutt 1985).

Decreasing the range still a bit more, we come into the shadow region of the x caustic. It is now interesting to look at the contours in this region. In Fig. 6 we have plotted the purely real solutions of $t = \theta$. We can see that we do not have two extrema any more. Still, when we evaluate the corresponding seismogram (Chapman) we have a smooth arrival as can be seen in Fig. 6(c). We shall come to this arrival just in a moment; first we also have a look at the complex solutions for the contour. In Fig. 6(b) we have plotted the non-real solutions for p which is now a contour which does not intersect the real p axis any more. It is a contour which has non-real solutions for all values of θ, before as well as after the arrival time at the (complex) saddle point. As for the curves in the lit region of the caustic, we can note from these curves that if we specify one time value t, we can always find three p values, one of which is real and two complex, the two complex ones being the complex-conjugates of each other.

Evaluating the complex solutions gives us the other seismogram as depicted in Fig. 6(c). We can compare the two methods and see that the methods compare very well; the waveforms are the same although the seismogram from the complex p values is slightly off-set by a DC-value in the pressure P.

For interpretational purposes it is interesting to know what the smooth arrival represents and what its approximate behaviour is. To this end, we expand about the complex value p_s which makes θ an extremum. Let $p = p_s + \varepsilon$, then

$$\theta \simeq \theta|_{p=p_s} + \frac{1}{2}\varepsilon^2 \frac{d^2\theta}{dp^2}\bigg|_{p=p_s} \tag{34}$$

$$= T_s + iE_s + \frac{1}{2}\varepsilon^2(u_1 + iu_2), \tag{35}$$

where T_s and E_s are the arrival time and the evanescence respectively, associated with the saddle-point value. It is interesting to note that the value p_s does not lie on any of the contours $t = \theta$. This is obvious since we require t to be real so we cannot expect to obtain p values which give a complex-valued arrival time. We have also called $d^2\theta/dp^2$ at the saddle-point value $(u_1 + iu_2)$ where u_1 and u_2 are real-valued. Solving for ε gives us

$$\varepsilon = 2^{1/2}\frac{(\theta - T_s - iE_s)^{1/2}}{(u_1 + iu_2)^{1/2}}. \tag{36}$$

We then expand $d\theta/dp$ around this value and substitute ε:

$$\frac{d\theta}{dp} \simeq \varepsilon \frac{d^2\theta}{dp^2}\bigg|_{p=p_s} \tag{37}$$

$$= 2^{1/2}(\theta - T_s - iE_s)^{1/2}(u_1 + iu_2)^{1/2}. \tag{38}$$

Using these expressions we have compared the terms $\mathcal{I}m(\ldots)$ in expression (31) as in Fig. 7. We have taken such a range that we are not too near to the caustic. We can see that the waveforms do look very much the same, the only difference being a DC value between the two. This means that the signal in the shadow part of the caustic can be interpreted as a contribution of complex or tunnelling rays, i.e., rays which give complex-valued arrival times and *complex-valued spreading factors (Keller & Karal 1960, 1964; Drijkoningen & Chapman 1988).*

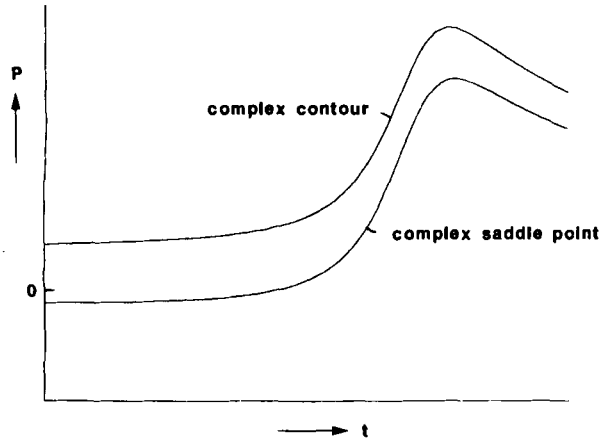

Figure 7. Comparison between Heyman–Felsen response and response using complex-saddle-point approximation.

We have compared the seismograms for the real and complex contours $t = \theta$, but using the complex solutions has the advantage that we do not have any endpoint errors which are intrinsic to Chapman's method (see, e.g., Thomson & Chapman 1986). Endpoint errors occur here due to the vertical slowness (q_1) becoming complex at the source and/or receiver.

So far, we only looked at the case of two saddle points forming a caustic, but going along all ranges shows that there are two caustics for the Epstein profile under consideration (solving $d^2\theta/dp^2 = 0$ gives two solutions). This can be seen in the T–x diagram (Fig. 4). The other caustic (point D in the T–x diagram) shows the same feature in as much that two arrivals merge into one. The way they merge here is different from before since one of the contours $t = \theta$ looks different. In Fig. 8 we have plotted the characteristic contours for this caustic. Fig. 8(a) shows the behaviour of the two contours in the lit region of the caustic, one being the one of a normal turning ray and one of a reversed turning ray. What is different here is that the curve for the normal turning ray comes from the 'right' of the complex p plane with increasing θ. In the shadow region of the caustic the two caustics also merge differently as can be seen in Fig. 8(b). With increasing θ, the curve comes from the 'right' and, going along the complex saddle point, the curve also leaves the picture to the 'right' of the complex p plane.

In Fig. 9, we finally show a complete set of seismograms with ranges which include both caustics. The traveltime as a function of range can be seen forming a triplication. Note also the relatively high amplitudes at the caustic due to focusing of two rays, adding two saddle-point contributions.

DISCUSSION

We have shown that a generalized ray theory approach can be used to obtain synthetic seismograms for reversed turning

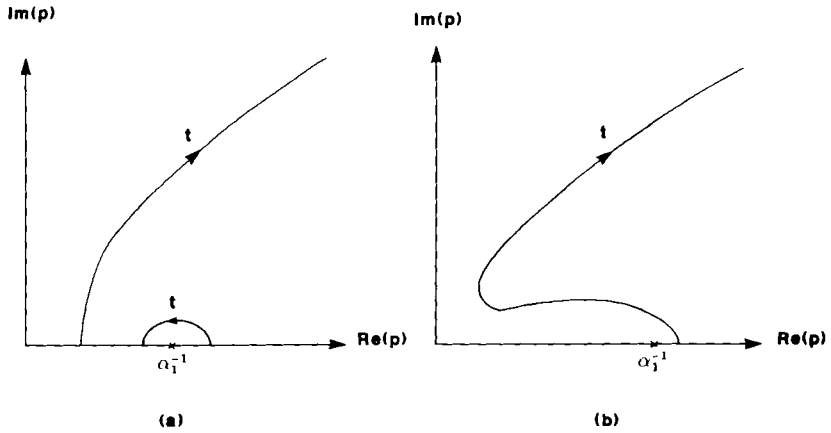

Figure 8. Complex contour for caustic at far end of triplication curve. (a) Lit region and (b) dark region of caustic.

rays and **x** caustics. The synthetics were generally quite accurate as comparisons with results from Chapman's inversion method show. What we haven't mentioned so far is that finding the non-real solutions for the contour θ is not a trivial matter. For each trace of the synthetics in the final pictures we needed to calculate two or three contours. When searching for these contours numerically we must guess the initial value in the iteration scheme judiciously. The procedure is not in any way subjective but is sometimes quite combersome. This makes the method less attractive when using it for more complicated structures. Chapman's inversion method can deal with these contour calculations much easier. With this method we choose a (real) p value and the θ function can be constructed by letting p increase *monotonically*. Going along the real p axis then gives the θ curve and we can construct the seismogram without much difficulty.

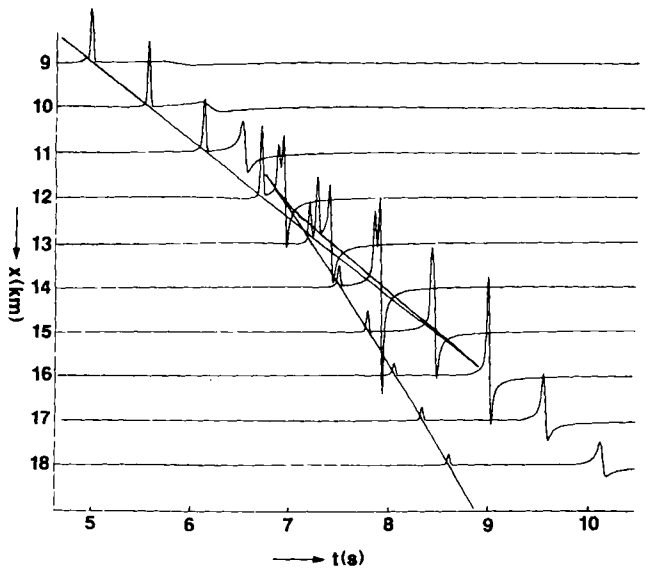

Figure 9. Synthetic seismograms for monotonic transition zone using complex solutions for $t = \theta$. $\alpha_1 = 1.7\,\mathrm{km\,s^{-1}}$, $\alpha_2 = 4\,\mathrm{km\,s^{-1}}$, $\sigma = 0.9$, $z_{source} = z_{receiver} = 4.45\,\mathrm{km}$.

CONCLUSIONS

In this paper we have shown how the method of Heyman & Felsen performs for an Epstein transition zone. The method is able to deal with normal turning rays, reversed turning rays and **x** caustics. The normal turning ray has all the characteristics of a geometrical arrival and the reversed turning ray has the characteristics of a Hilbert-transformed geometrical arrival. At the caustic the waveform is the inverse Fourier transform of the Airy function but with the method employed here, the waveform is built up in an automatic fashion. In the dark region of the caustic we showed that the arrival can be associated with tunnelling rays, i.e., rays with complex-valued 'arrival' times and complex geometrical spreading factors. The results obtained with this method compared favourably with Chapman's (WKBJ seismogram) method. The waveforms were identical, a difference showing up only in the form of a DC value in the amplitude. However, this will not affect the results unduly. A slight advantage of Heyman–Felsen's method over Chapman's method is that it does not have any endpoint errors, intrinsically present in Chapman's method. However, this advantage may be outweighed by the advantage of Chapman's method in dealing with more complicated structures than investigated here.

ACKNOWLEDGMENTS

The author wishes to thank professor Chris Chapman for pointing out the usefulness of investigating the Epstein profile with the Heyman–Felsen method. Thanks are also due to John Hudson who made some useful comments on the formulation of the method. The author was supported by a SHELL Scholarship at the University of Cambridge. Computations were performed at the VAX computer centre at the Bullard Laboratories, Department of Earth Sciences, Cambridge. Department of Earth Sciences publication no. 1776.

REFERENCES

Abramowitz, M. & Stegun, I. A., 1972. *Handbook of Mathematical Functions*, Dover, New York.

Aki, K. & Richards, P. G., 1980. *Quantitative Seismology*, vol. I, W. H. Freeman, San Francisco.

Budden, K. G., 1961. *Radio Waves in the Ionosphere*, Cambridge University Press, Cambridge, UK.

Burridge, R., 1963. The reflexion of a disturbance within an elastic sphere, *PhD thesis*, University of Cambridge, Cambridge, UK.

Chapman, C. H., 1978. A new method for computing synthetic seismograms, *Geophs. J. R. astr. Soc.*, **64**, 481–518.

Chapman, C. H. & Drummond, R., 1982. Body-wave seismograms in inhomogeneous media using Maslov asymptotic theory, *Bull. seism. Soc. Am.*, **72**, S277–S317.

Chapman, C. H. & Orcutt, J. A., 1985. The computation of body wave synthetic seismograms in laterally homogeneous media, *Rev. Geophys.*, **23**, 105–163.

Chapman, C. H., Jen-Yi, C. & Lyness, D. G., 1988. The WKBJ seismogram algorithm, in *Seismological Algorithms: Computational Methods and Computer Programs*, ed. Doornbos, D. J., Academic Press, London.

Dey-Sarkar, S. K. & Chapman, C. H., 1978. A simple method for the computation of body wave seismograms, *Bull. seism. Soc. Am.*, **68**, 1577–1593.

Drijkoningen, G. G., 1989. On generalized ray theory in inhomogeneous media, *PhD thesis*, Cambridge, UK.

Drijkoningen, G. G. & Chapman, C. H., 1988. Tunneling rays using the Cagniard–de Hoop method, *Bull seism. Soc. Am.*, **78**, 898–907.

Epstein, P. S., 1930. Reflection of waves in an inhomogeneous absorbing medium, *Proc. Nat. Acad. Sci. Wash.*, **16**, 627–637.

Heyman, E. & Felsen, L. B., 1984. Non-dispersive approximation for transient ray fields in an inhomogeneous medium, in *Hybrid Formulation of Wave Propagation and Scattering*, NATO ASI, Series E, no. 86, pp. 269–284, ed. Felsen, L. B., Nijhoff.

Heyman, E. & Felsen, L. B., 1987. Real and complex spectra—a generalization of WKBJ seismograms, *Geophs. J. R. astr. Soc.*, **91**, 1087–1126.

Hong, T.-L. & Helmberger, D. V., 1977. Generalized ray theory for dipping structure, *Bull. seism. Soc. Am.*, **67**, 995–1008.

Hong, T.-L. & Helmberger, D. V., 1978. Glorified optics and wave propagation in nonplanar structure, *Bull. seism. Soc. Am.*, **68**, 1313–1330.

Hron, M. & Chapman, C. H., 1974. Seismograms from Epstein transition zones, *Geophys. J. R. astr. Soc.*, **37**, 305–322.

Jeffreys, H., 1939. The time on core waves, *Mon. Not. R. astr. Soc., Geophys. Suppl.*, **4**, 548–561.

Keller, J. B. & Karal, F. C., 1960. Surface wave excitation and propagation, *J. appl. Phys.*, **31**, 1039–1046.

Keller, J. B. & Karal, F. C., 1964. Geometrical theory of elastic surface-wave excitation and propagation, *J. acoust. Soc. Am.*, **36**, 32–40.

Maslov, V. P., 1965. *Theory of Perturbations and Asymptotic Methods*, Izd. MGU, Moscow (in Russian).

Maslov, V. P., 1972. *Théory des Perturbations et Méthodes Asymptotiques*, Dunods, Paris.

Phinney, R. A., 1970. Reflection of acoustic waves from a continuously varying interfacial region, *Rev. Geophys. Space Phys.*, **8**, 517–532.

Thomson, C. J. & Chapman, C. H., 1986. End-point contributions to synthetic seismograms, *Geophys. J. R. astr. Soc.*, **87**, 285–294.

Ziołkowski, R. W. & Deschamps, G. A., 1984. Asymptotic evaluation of high frequency fields near a caustic: an introduction to Maslov's method, *Radio Sci.*, **19**, 1001–1025.